Water-resistant perovskite-inspired copper/silver pnictohalide nanocrystals for photoelectrochemical water splitting

Maning Liu [a,e,*], G. Krishnamurthy Grandhi [a], Basheer Al-Anesi [a], Harri Ali-Löytty [b], Kimmo Lahtonen [c], Roberto Grisorio [d], Paola Vivo [a,*]

[a] *Hybrid Solar Cells, Faculty of Engineering and Natural Sciences, Tampere University, P.O. Box 541, FI-33014 Tampere University, Finland*
[b] *Surface Science Group, Photonics Laboratory, Tampere University, P.O. Box 692, FI-33014 Tampere University, Finland*
[c] *Faculty of Engineering and Natural Sciences, Tampere University, P.O. Box 692, FI-33014 Tampere, Finland*
[d] *Dipartimento di Ingegneria Civile, Ambientale, del Territorio, Edile e di Chimica (DICATECh), Politecnico di Bari, 70125 Bari, Italy*
[e] *Centre for Analysis and Synthesis, Lund University, P.O. Box 124, 22100 Lund, Sweden*

ARTICLE INFO

ABSTRACT

Lead halide perovskites (LHPs) photoelectrodes for photoelectrochemical (PEC) water splitting are promising candidates for solar-to-fuel conversion. However, the poor stability of LHPs in aqueous electrolyte media, together with the toxicity of lead, restricts the practical application of LHP photoelectrodes. Herein, we report the first-ever colloidal synthesis of quaternary $Cu_{1.4}Ag_{0.6}BiI_5$ nanocrystals (NCs), a new lead-free perovskite-inspired nanomaterial, by a facile hot injection method. The $Cu_{1.4}Ag_{0.6}BiI_5$ NCs exhibit an extraordinary water resistance, due to the well-defined coverage of hydrophobic ligands on the surface of NCs with unique layered cation disordered structure. Together with their high structural stability, the $Cu_{1.4}Ag_{0.6}BiI_5$ NCs-based photoanode displays a maximum photocurrent density of 4.62 mA cm^{-2} at 1.23 V vs. reversible hydrogen electrode, and an applied bias photo-to-current efficiency of 2.94% without any protective layer. Our study highlights the great potential of lead-free $Cu_{1.4}Ag_{0.6}BiI_5$ NCs-based photoelectrodes for a wide range of low-cost, eco-friendly, and high-performance PEC applications.

Solar water splitting is one of the most promising techniques to convert and store the abundant solar energy into hydrogen [1,2]. Of the diverse types of water splitting systems, photoelectrochemical (PEC) water splitting is of great interest for hydrogen generation [3,4]. Just over the last few years, lead (Pb) halide perovskites (LHPs) have been considered as attractive photoelectrodes for PEC reactions [5–7], due to their high light absorption coefficient ($\sim 10^5$ cm^{-1}), long charge diffusion length (>1 μm), and high charge carrier mobility (1–10 cm^2 V^{-1} s^{-1}) [8–11]. To date, the solar-to-hydrogen conversion efficiency of LHP-based photoelectrodes has surpassed 11% [12]. Although enormous efforts have been made to design and fabricate various types of LHP-based photoelectrodes, the strict fabrication environment, particularly the need of insulate the LHP active layer from water and oxygen with the help of protective catalytic layers [5,13,14], has still limited the application of LHP-based PEC water splitting. The considerable instability weakness of LHPs, accompanied with the high toxicity of Pb element, makes the discovery of stable Pb-free alternatives for efficient PEC reactions highly desirable.

Pb-free perovskite-inspired materials (PIM) [15] such as copper or silver pnictohalides with a typical structure $A_xB_yX_{x+3y}$ (A = Cu$^+$, Ag$^+$; B = Bi^{3+}, Sb^{3+}; X = I^-), e.g., CuBiI$_4$, Cu$_2$BiI$_5$ and Ag$_3$BiI$_6$ [16], have gained growing attention for diverse optoelectronic and photocatalytic applications [17–20], owing to their low toxicity, various structural dimensionality, and wide tunability of band gap. Recently, ternary copper pnictohalides (e.g., CuBiI$_4$) have been found to exhibit a metastable phase that can decompose to CuI and BiI$_3$ even at room temperature [21]. To tackle this phase stability issue, the quaternary Cu-Ag-Bi-I system has been investigated with a focus on Cu$_2$AgBiI$_6$ [22], demonstrating a direct band gap (2.06–2.10 eV) [23,24] with a very high absorption coefficient (>1×10^5 cm^{-1}) that is comparable to that of LHPs. So far, Cu$_2$AgBiI$_6$ thin film has only been employed in the photovoltaic and photodetector applications [23], showing moderate power conversion efficiencies of 1.3% under 1 sun condition and 4.7% under indoor illumination ($\sim$1000 lx) [24]. The reported good optical properties and high structural stability of lead-free quaternary Cu-Ag-Bi-I semiconductor along with its suitable band gap ($\sim$2 eV) may open up another

* Corresponding author.
E-mail addresses: maning.liu@tuni.fi (M. Liu), paola.vivo@tuni.fi (P. Vivo).

possibility to be favorable for the PEC water splitting. On the other hand, very few studies on robust and water-resistant halide perovskites or PIMs for PEC applications without any protective or encapsulation layers, have been reported [25,26].

Herein, we report the colloidal synthesis of lead-free quaternary $Cu_{1.4}Ag_{0.6}BiI_5$ NCs for the first time. The NCs exhibit an exceptional water resistance, which we ascribe to the well-defined coverage of hydrophobic ligands on the surface of NCs with layered cation disordered structure. The as-synthesized $Cu_{1.4}Ag_{0.6}BiI_5$ NCs demonstrate a relatively long photoluminescence (PL) lifetime of ~48 ns with a middle direct band gap of 2.19 eV and band structures well aligned with the redox potentials of water splitting reaction. For a proof-of-concept application, the simplified PEC cell, fabricated with the $Cu_{1.4}Ag_{0.6}BiI_5$ NCs film as the photoanode in the absence of a protective layer, exhibits -0.05 V_{RHE} (RHE = reversible hydrogen electrode) onset potential and a maximum photocurrent density of 4.62 mA cm^{-2} at 1.23 V_{RHE}, as well as an applied bias photon-to-current efficiency (ABPE) of 2.94%. We further investigate the reaction dynamics of photogenerated charge carriers in $Cu_{1.4}Ag_{0.6}BiI_5$NCs with water molecules by conducting ultrafast transient absorption (TA) measurements, revealing that the population of electrons in $Cu_{1.4}Ag_{0.6}BiI_5$ NCs dominates the charge carrier (electron-hole) recombination during the water splitting reaction.

The Pb-free quaternary Cu-Ag-Bi-I NCs were synthesized according to a modified hot injection method (see the synthesis details in the Supporting Information, SI) [27,28]. It is noteworthy that the production yield is quite high (>95%) upon the injection of TMS-I into the metal acetate-based precursor, suggesting that the separation of the halide source (I^-) from the metal cation source (Cu^+, Ag^+, and Bi^{3+}) is more favorable for the swift formation of nuclei compared to the conventional metal-oleate injection method. The X-ray diffraction (XRD) pattern (Fig. 1a) of the as-synthesized Cu-Ag-Bi-I NCs reveals the formation of a trigonal structure with a space group of $R\bar{3}m$, in agreement with the reported reference patterns of Cu_2BiI_5 single crystals and bulk crystals [29], hinting that as-formed Cu-Ag-Bi-I NCs demonstrate a featured structure of defect spinel-type $A_2B_1\times_5$ material[16] with partial occupancy of Ag^+ at A site. It is noted that the adjoining characteristic peaks at $2\theta = 41.7°$ and $42.1°$ in the reference pattern of Cu_2BiI_5 single crystals merge into one wider peak at $2\theta = 42.0°$ in the pattern of Cu-Ag-Bi-I NCs, which is also observed in the case of reported Cu_2BiI_5 bulk crystals, likely due to the reduced crystallinity in the form of bulk- and nanocrystals compared to their analogous single crystals. One minor characteristic peak is detected in the XRD pattern of Cu-Ag-Bi-I NCs, i.e., 26.8°, attributed to the residual or decomposed BiI_3 impurities [29]. Besides, there is no clear shift in the Bragg angles of Cu-Ag-Bi-I NCs compared to those of the reference pattern (i.e., Cu_2BiI_5 single crystals), suggesting that the involvement of Ag^+ with Cu^+ at A site hardly alters the lattice constants, owing to the similarity of Cu^+ (0.5 Å) and Ag^+ (0.6 Å) ionic radii [30]. We, thus, defined our quaternary Cu-Ag-Bi-I NCs as $Cu_{2-x}Ag_xBiI_5$. To further determine the x value for the Ag content, we conducted the elemental analysis including the energy-dispersive X-ray spectroscopy (EDS) and inductively coupled plasma mass spectroscopy (ICP-MS). The EDS mapping images in Fig. 1b validate the homogeneous distribution of Cu, Ag, Bi, and I elements in $Cu_{2-x}Ag_xBiI_5$ NCs. The EDS analysis confirms the actual elemental ratios of Cu:Ag:Bi:I as 1.29:0.43:1.01:5.00, while the ICP-MS analysis further verifies the molar ratio of metal cations, i.e., Cu:Ag:Bi = 1.20:0.53:1.32 (Table 1). Thus, we determined the $x = 0.6$ by averaging the bulky elemental ratios
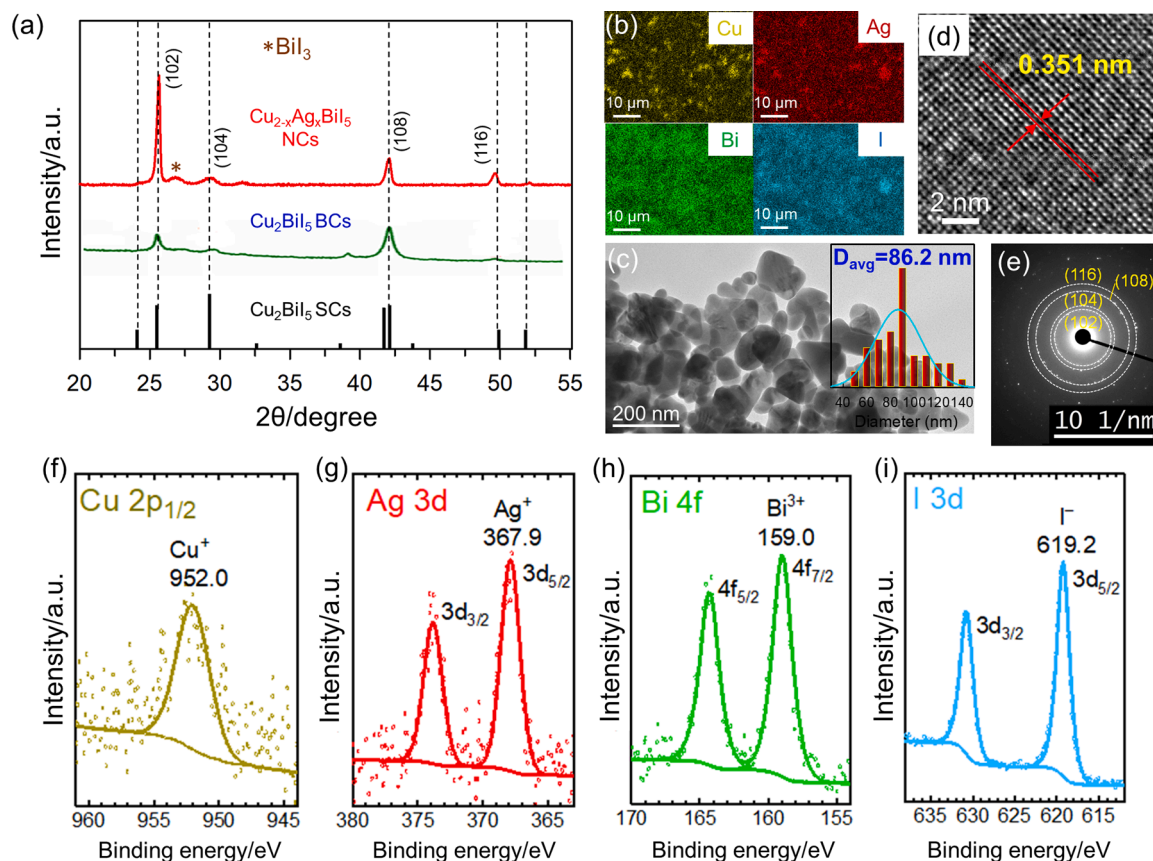

Fig. 1. (a) XRD pattern of as-synthesized Cu-Ag-Bi-I NCs compared with the XRD pattern of the reported reference patterns of Cu_2BiI_5 bulk crystals (BCs)[29] and single crystals (SCs, JCPDS#00–046–0608). (b) EDS mapping images of Cu-Ag-Bi-I NCs. (c) TEM and (d) High-resolution TEM (HRTEM) images of $Cu_{1.4}Ag_{0.6}BiI_5$ NCs. A size distribution histogram in (b) shows an average diameter of 86.2±23.5 nm. (e) SAED pattern for the TEM image of $Cu_{1.4}Ag_{0.6}BiI_5$ NCs. (f) Cu 2p$_{1/2}$, (g) Ag 3d, (h) Bi 4f, and (i) I 3d XPS spectra of $Cu_{1.4}Ag_{0.6}BiI_5$ NCs.

Table 1
Elemental analysis for $Cu_{2-x}Ag_xBiI_5$ NCs.

Analytical method	Element			
	Cu	Ag	Bi	I
EDS	1.29	0.43	1.01	5.00
ICP-MS	1.20	0.53	1.32	–

of Cu:Ag extracted from both EDS and ICP-MS results, leading to the stoichiometry of $Cu_{1.4}Ag_{0.6}BiI_5$. This indicates that ~70% of Cu^+ cations have been successfully alloyed with ~30% of Ag^+ cations at A site to form a layered cation mixed structure. It is notable that the elemental ratio (1.3) of (Cu+Ag)/Bi is fairly lower than the nominal value (2.0) based on the ICP-MS data, plausibly due to the partial replacement of surface Cu^+ and Ag^+ by the organic cations such as oleylammonium ions (OAm^+), which has been widely reported for the observed deficiency of Cs^+ cation in the ratio (<1) of Cs/Pb in the lead-based perovskite NCs (e. g., $CsPbX_3$ NCs) [31].

The transmission electron microscopy (TEM) image presented in Fig. 1c shows that the $Cu_{1.4}Ag_{0.6}BiI_5$ NCs are in a prism-like shape with an average diameter of 86.2±23.5 nm. The high-resolution TEM (HRTEM) image (Fig. 1d) demonstrates a highly crystalline structure with a lattice D-spacing of 0.351 nm, which is assigned to the (102)

crystal plane, in agreement with the crystalline direction determined from the selected area electron diffraction (SAED) pattern (Fig. 1e). All these together with the previous XRD data (Fig. 1a) further verify a trigonal crystal structure. To gain insight into the surface chemistry of $Cu_{1.4}Ag_{0.6}BiI_5$ NCs, we conducted the X-ray photoelectron spectroscopy (XPS) measurements. Only one chemical state was resolved for Cu (Cu $2p_{1/2}$ at 952.0 eV), Ag (Ag $3d_{5/2}$ at 367.9 eV), Bi (Bi $4f_{7/2}$ at 159.0 eV) and I (I $3d_{5/2}$ at 619.2 eV), which can be attributed to Cu^+, Ag^+, Bi^{3+} and I^-, respectively [32] (Fig. 1f-i).

We further investigated the optical properties of as-synthesized $Cu_{1.4}Ag_{0.6}BiI_5$ NCs, e.g., band gap, which is crucial to evaluate the potential for the photocatalytic activity. Our Tauc analysis for the absorption spectrum (Fig. 2a) indicates the nature of direct band gap obtained for $Cu_{1.4}Ag_{0.6}BiI_5$ NCs, consistent with the Cu_2BiI_5 bulk case reported previously [29]. The extracted band gap (2.19 eV) of $Cu_{1.4}Ag_{0.6}BiI_5$ NCs is larger than those reported 1.53–1.74 eV and 2.06–2.10 eV for the Cu_2BiI_5 thin films[29] and Cu_2AgBiI_6 thin films [22,23], respectively, which is also higher than the required minimum band gap (1.23 eV) for potential water splitting reaction [33]. The corresponding PL spectrum of $Cu_{1.4}Ag_{0.6}BiI_5$ NCs (Fig. 2a) demonstrates an absolute PL quantum yield (PLQY) of 1.1%, with a relatively broad (full width at half maximum, FWHM = 430 meV) and tilted spectral
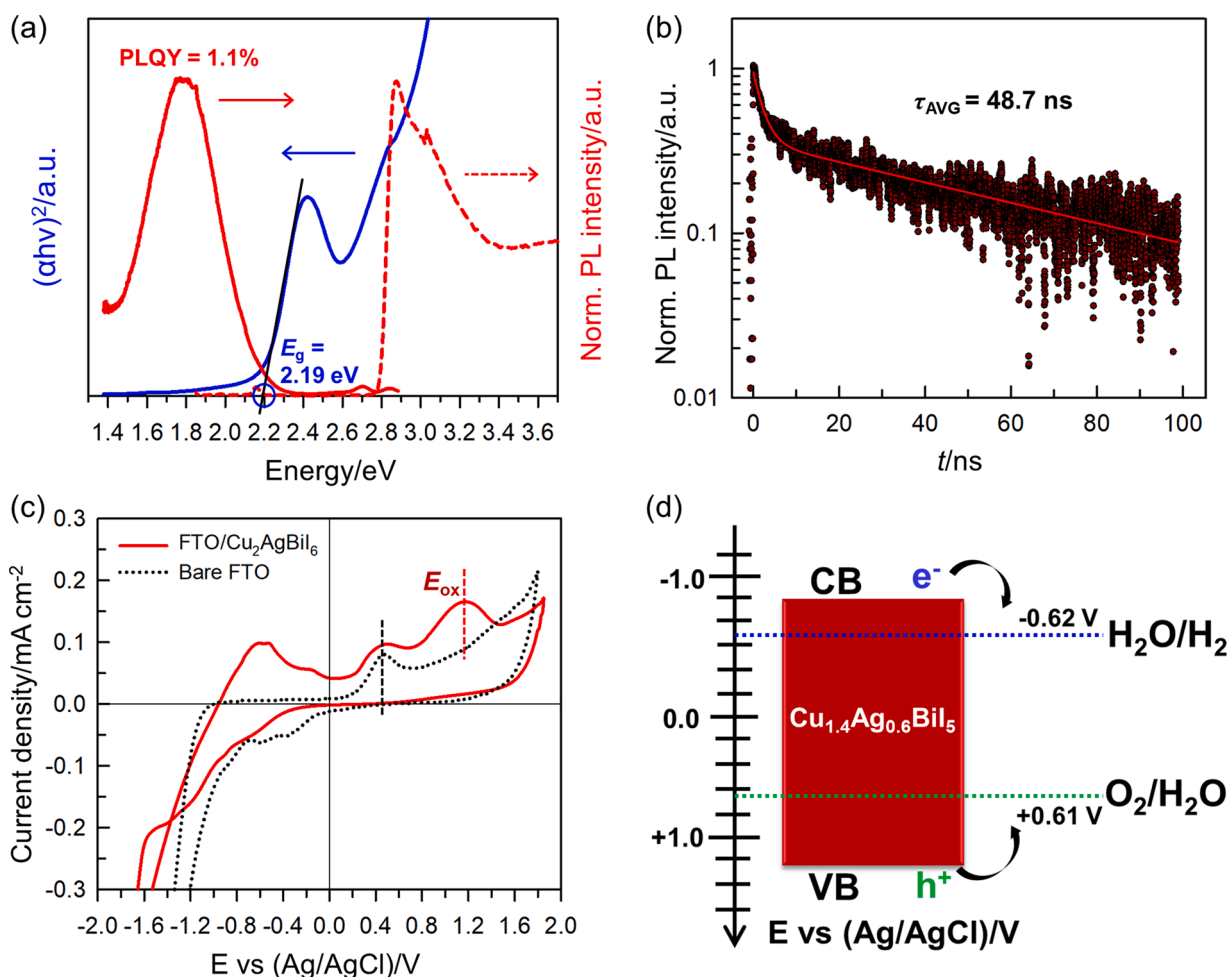

Fig. 2. (a) PL and PL excitation (PLE) spectra of $Cu_{1.4}Ag_{0.6}BiI_5$ NCs in suspension, excited at 405 nm and monitored at 695 nm, along with the Tauc plot of the steady-state absorption spectrum of $Cu_{1.4}Ag_{0.6}BiI_5$ NCs. (b) Time-resolved PL (TRPL) decay of $Cu_{1.4}Ag_{0.6}BiI_5$ NCs in suspension, excited at 405 nm. The solid line shows the fitting result with a stretched exponential function: $I = I_0 e^{-(t/\tau)^a}$. (c) Cyclic voltammograms of Fc/Fc^+ standard (dotted line) and $Cu_{1.4}Ag_{0.6}BiI_5$ NCs film coated on FTO substrate (solid line) as working electrode (WE) in 0.1 M Bu_4NPF_6 electrolyte in dichloromethane, while a Pt wire and Ag/AgCl electrode are the counter electrode (CE) and reference electrode (RE), respectively. The reduction potential (V_e) and oxidation potential (V_h) positions of $Cu_{1.4}Ag_{0.6}BiI_5$ NCs film are highlighted with red dashed lines while the redox potential peaks of Fc/Fc^+ are highlighted with blue dashed lines. (d) Potential level diagram of $Cu_{1.4}Ag_{0.6}BiI_5$ NCs film in aqueous solution at pH 7. The reduction potential of hydrogen generation and the oxidation potential of oxygen generation from water are also presented [36].

shape as well as a long PL tail beyond 1.4 eV The observed large redshift of PL peak position (1.78 eV) compared to the first excitonic peak (2.42 eV) is ascribed to the formation of self-trapped excitons (STEs), which has been previously claimed for quaternary Cu-Ag-Bi-I bulk materials [23,34]. This may also possibly explain the mismatch between PL excitation (PLE) spectrum and absorption spectrum (Fig. 2a), hinting that the $Cu_{1.4}Ag_{0.6}BiI_5$ semiconductor can absorb and convert sub-band gap light due to the existence of STE states. To determine the lifetime of $Cu_{1.4}Ag_{0.6}BiI_5$ NCs in their excited state, we measured the time-resolved PL (TRPL) decay for $Cu_{1.4}Ag_{0.6}BiI_5$ NCs in suspension (Fig. 2b), which was excited at 405 nm and monitored at 695 nm. The TRPL decay was fitted with a stretched exponential function: $I = I_0 e^{-(t/\tau)^\alpha}$, where α is the distribution coefficient and τ is the effective lifetime when the PL intensity drops to I_0/e [22]. The fitting ($\alpha = 0.32$ and $\tau = 6.9$ ns) yields an average lifetime (τ_{avg}) of 48.3 ns, which is even longer than the reported (33 ns) for quaternary Cu-Ag-Bi-I in the form of bulk crystals [22]. This may suggest that, compared to the bulk phase, the trap distribution on the $Cu_{1.4}Ag_{0.6}BiI_5$ surface is more homogeneous in the form of NCs with the help of surface ligands, leading to the extension of radiative recombination lifetime [35]. The key optical properties of $Cu_{1.4}Ag_{0.6}BiI_5$ NCs are summarized in Table 2.

The appropriate band position, i.e., conduction band minimum (CBM) and valence band maximum (VBM), plays a significant role in realizing an efficient photocatalytic system. We, thus, clarified the band structures of $Cu_{1.4}Ag_{0.6}BiI_5$ NCs by conducting electrochemical measurements (i.e., cyclic voltammetry) in a three-electrode cell system [37, 38] (see the experimental details in the SI). The redox potential of $Cu_{1.4}Ag_{0.6}BiI_5$ NC film on an FTO substrate as the working electrode (WE) can be determined based on the recorded cyclic voltammograms by comparing with a ferrocene/ferrocenium (Fc/Fc⁺) standard in Fig. 2c. The reduction potential (V_e) and oxidation potential (V_h) irreversible peaks for the $Cu_{1.4}Ag_{0.6}BiI_5$ NCs film were extracted as -0.78 and 1.23 V, respectively. The energy level of Fc/Fc⁺ standard was determined as -4.8 eV vs. vacuum [38]. We then calculated the conduction band (E_{CB}^{ec}) and valence band (E_{VB}^{ec}) as $E_{CB}^{ec} = -[V_e-V(Fc/Fc^+)+4.8]eV = -[-0.78-(0.1+0.3)/2+4.8]eV = -3.82$ eV, and $E_{VB}^{ec} = -[V_h-V(Fc/Fc^+)+4.8]eV = -[1.23-(0.1+0.3)/2+4.8]eV = -5.83$ eV, thus the electrochemical band gap can be estimated as $E_g^{ec} = (5.83-3.82)$ eV $= 2.01$ eV It is noted that the E_g^{ec} (2.01 eV) is lower than the E_g^{opt} (2.19 eV) determined by the Tauc analysis. Due to the observed large STE states that dominate the band-edge optical transitions, the Tauc analysis may overestimate the optical band gap, therefore, the E_g^{ec} (2.01 eV) is more reliable to describe the direct band-to-band transition for the $Cu_{1.4}Ag_{0.6}BiI_5$ NCs. All the evaluated electrochemical properties of $Cu_{1.4}Ag_{0.6}BiI_5$ NCs are also included in Table 2. Fig. 2d depicts the calculated band structures of $Cu_{1.4}Ag_{0.6}BiI_5$ NCs with respect to the standard redox potentials for the water splitting reaction, confirming that $Cu_{1.4}Ag_{0.6}BiI_5$ NCs have suitable energy level alignments (VB and CB) to realize the photooxidation for oxygen evolution as well as the photoreduction for hydrogen evolution.

It is crucial to meet the stability requirements for metal halide perovskites-based photoelectrode for their PEC water splitting

application, since most of halide perovskite materials can quickly decompose after immersing in aqueous electrolytes. Therefore, a water-resistant and conductive layer is generally coated atop the halide perovskite photoelectrode as a protective layer in the PEC cell [13,14]. We investigated the solvent stability of $Cu_{1.4}Ag_{0.6}BiI_5$ NCs film by immersing in different solvents, namely water, methanol, ethanol, and 2-propanol (see Fig. S2 in the SI). Surprisingly, the $Cu_{1.4}Ag_{0.6}BiI_5$ NCs film can sustain well only in water while dissolving swiftly in other solvents within 10 min after immersing. This is possibly due to the insolubility of hydrophobic capping ligands in water that in turn can be dissolved in alcohol solvents. The NC film showed no obvious change in the appearance even up to 7 h of immersion in water (see the inset photos in Fig. 3a), also as evident by the nearly identical XRD patterns (Fig. 3a) that confirm the superior structural stability of $Cu_{1.4}Ag_{0.6}BiI_5$ NCs film in water. The surface hydrophobicity of $Cu_{1.4}Ag_{0.6}BiI_5$ NCs film was further clarified by measuring the water contact angles (mean = 85.6 °) of glass/$Cu_{1.4}Ag_{0.6}BiI_5$ NCs sample (Fig. 3b), which are much larger than the reported CA (<57.6°) for quaternary Cu-Ag-Bi-I bulk film without capping ligands [23]. We thus attribute the unique water-resistant property to the well-defined coverage of water-insoluble capping ligands, i.e., OA and OAm, on the surface of $Cu_{1.4}Ag_{0.6}BiI_5$ NCs with layered cation disordered structure (see the hypothesized scheme in Fig. 3c and surface analysis in Fig. S1a-b in the SI). It is also noted that the strong C—C/H peak in the XPS spectra can be partially assigned to the capping ligands (OA and OAm), which contain long C—C chains by showing high surface concentration of carbon (76.3 at.%). To quantitatively assess the amount of organic capping ligands (OA and OAm) on the NC core, we conducted the thermogravimetric analysis (TGA) measurements for the as-synthesized $Cu_{1.4}Ag_{0.6}BiI_5$ NCs (see the TGA curve in Fig. S1c in the SI). We note two distinguishable stages for the weight loss in the TGA curve. We attribute the stage I to the loss (~68.9 wt% until 420 °C) of the organic binder, i.e., organic capping ligands (OA and OAm), and the stage II to the decomposition (~30.4 wt% until 845 °C) of the inorganic $Cu_{1.4}Ag_{0.6}BiI_5$ cores. We can thus estimate the molar ratio between organic capping ligands (OA and OAm) and inorganic cores ($Cu_{1.4}Ag_{0.6}BiI_5$) as approximately 10:1, based on their corresponding weight losses. This indicates that ten parts of OA and OAm molecules are required to effectively stabilize one part of $Cu_{1.4}Ag_{0.6}BiI_5$ NC cores. On the other hand, it has been reported that a super-hydrophobicity can be achieved through the adsorption of atmospheric volatile organic compounds (VOCs) on the micro/nanostructured metal oxide nanocrystal surfaces [39]. This provides significant hints for our work that the unique layered nanostructured $Cu_{1.4}Ag_{0.6}BiI_5$ NC surfaces may govern efficient adsorption of VOCs from the atmosphere, which also favors the high water-resistant property. Moreover, the air stability of $Cu_{1.4}Ag_{0.6}BiI_5$ NCs film was monitored by measuring the XRD patterns of the same NCs sample in its fresh and aged cases (Fig. S3), respectively. The intensity of the primary characteristic peak at 25.3° can retain above 85% of the initial value after 36 days of storage in air (RH~40%), indicating a relatively high structural stability of $Cu_{1.4}Ag_{0.6}BiI_5$ NCs in ambient conditions.

Inspired by the observed high water-resistant characteristic and

Table 2
Optical and electrochemical properties of as-synthesized $Cu_{1.4}Ag_{0.6}BiI_5$ NCs.

NCs	a) λ_{abs} /eV	b) λ_{PL} /eV	c) FWHM /meV	PLQY /%	d) E_g^{opt} /eV	e) E_g^{ec} /eV	E_{CB}^{ec} /eV	E_{VB}^{ec} /eV	f) τ_{avg} /ns
$Cu_{1.4}Ag_{0.6}BiI_5$	2.42	1.78	430	1.1	2.19	2.01	3.82	5.83	48.7

a) First exciton peak

b) Emission peak

c) Full width at half maximum.

d) Optical band gap.

e) Electrochemical band gap.
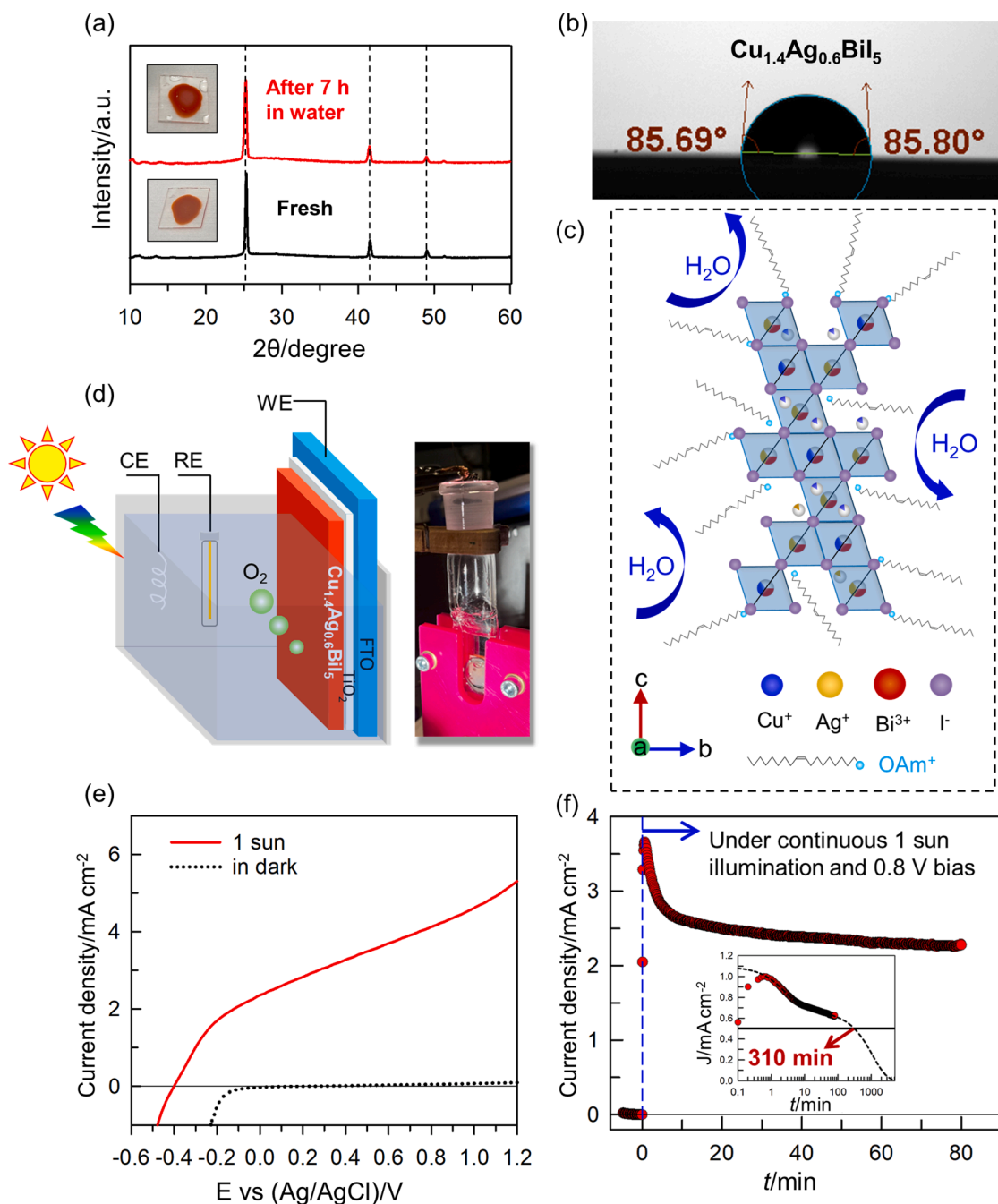
f) Average PL lifetime.

Fig. 3. (a) Comparison of XRD patterns of $Cu_{1.4}Ag_{0.6}BiI_5$ NCs film before and after immersing in water for 7 h (b) Water contact angles (CAs) of $Cu_{1.4}Ag_{0.6}BiI_5$ NCs film coated on glass. (c) Schematic illustration of water-insoluble ligands (oleic acid (OA) and oleylamine (OAm))-capped $Cu_{1.4}Ag_{0.6}BiI_5$ NC with layered cation disordered structure. (d) Scheme of water oxidation of $Cu_{1.4}Ag_{0.6}BiI_5$ NCs-based photoanode for PEC oxygen evolution. A side photo shows a typical assembling of one PEC cell. (e) Current density (J)–applied potential difference (V) of a $Cu_{1.4}Ag_{0.6}BiI_5$ NCs-based photoelectrode under 1 sun illumination (AM 1.5 G, 100 mW cm^{-2}) or in dark. The data were recorded by sweeping the applied potential difference from +1.4 V to –0.6 V vs. Ag/AgCl. The area of the photoelectrode that was exposed to the electrolyte is 0.785 cm^2. (f) Time course of current density of the $Cu_{1.4}Ag_{0.6}BiI_5$ NCs-based photoanode for oxygen generation under continuous 1 sun illumination and 0.8 V bias. Inset presents the linear projection of the stability trend to extract the $T_{50\%}$ lifetime (~310 min) of the photoelectrode, which corresponds to the time when the current density decreases to half of the initial value.

structural stability of $Cu_{1.4}Ag_{0.6}BiI_5$ NCs film, we fabricated simplified PEC cells with *n-i-p* configuration comprising FTO/TiO$_2$/Cu$_{1.4}$Ag$_{0.6}$BiI$_5$ NCs (see the cell schematic in Fig. 3d) without any protective layer (see the fabrication details in the SI), aiming to realize the direct photo-oxidation for oxygen generation. Following the current density (J)–applied potential difference (V) curve in Fig. 3e, the photocurrent generation of 4.62 mA cm^{-2} was recorded under 1-Sun illumination (100 mW cm^{-2}) at +1.03 $V_{Ag/AgCl}$ (equal to +1.23 V_{RHE}), with an onset

potential of –0.25 $V_{Ag/AgCl}$ (i.e., –0.05 V V_{RHE}). To quantitively assess the actual oxygen evolution reaction performance, the ABPE was calculated by the following Equation (1)[41]:

$$ABPE(\%) = \left(\frac{J_P \times (1.23 - V_b)}{P_{in}} \right) \times 100\% \tag{1}$$

where J_P is the photocurrent density (mA cm^{-2}) at the applied bias V_b (V), and P_{in} is the incident light intensity (mW cm^{-2}). The maximum

ABPE of our $Cu_{1.4}Ag_{0.6}BiI_5$ NCs-based PEC cells is 2.94% at 0.14 $V_{Ag/AgCl}$, to the best of our knowledge, which is the highest value among all reported Pb-free perovskites- or PIMs-based photoanodes for oxygen evolution (Table S1). This suggests that the water-resistant semiconducting $Cu_{1.4}Ag_{0.6}BiI_5$ NCs are energetically suitable as the photoelectrode for efficient PEC water splitting reaction. On the other hand, the obtained ABPE (2.94%) of our $Cu_{1.4}Ag_{0.6}BiI_5$ NCs-based PEC cells is still far behind the state-of-the-art value (9.16%) [40] achieved from the lead halide perovskites (bulk crystals)-based photoelectrodes, possibly due to the long alkyl chain capping ligands (e.g., OA) on the surface of NCs which can hinder the charge transfer for efficient oxidation reaction. This, in turn, requests further ligand engineering on the surface of $Cu_{1.4}Ag_{0.6}BiI_5$ NCs to optimize the charge transfer while still maintaining the high water-resistance. We then investigated the stability of the $Cu_{1.4}Ag_{0.6}BiI_5$ NCs-based PEC cell by measuring the time course of current density of the NCs-based photoanode for oxygen generation under continuous 1 sun illumination and 0.8 V bias (Fig. 3f). We extracted an estimated $T_{50\%}$ lifetime of ~310 min that corresponds to the time when the current density decreases to half of the initial value, based on a linear projection of the stability trend from the peak current density point (see the inset in Fig. 3f). We achieve one of the longest reported lifetimes when compared to other studies on both Pb-based and Pb-free perovskites or PIM nanocrystal-based photoelectrodes [26,41, 42].

To gain further insights into the reaction dynamics of photogenerated charge carriers (i.e., electrons and holes) in $Cu_{1.4}Ag_{0.6}BiI_5$ NCs with water molecules, we conducted a series of ultrafast TA measurements for the $Cu_{1.4}Ag_{0.6}BiI_5$ NCs film under various conditions. Fig. 4a shows the TA spectra of $Cu_{1.4}Ag_{0.6}BiI_5$ NCs film in air, which was excited at 400 nm. Two negative bands centered at ~450 and ~550 nm, correspond to the ground state bleaching (GSB) at the second and first excitonic bands. The strong GSB signal with 550 nm peak interrupts a broad positive photoinduced absorption (PIA) band from ~500 nm towards beyond 740 nm, with the latter wavelength being the limitation of our visible range detector. We attribute this broad PIA band to the STEs in their excited state, which has also been observed for other types of Pb-free perovskite NCs [28,43]. In comparison, as shown in Fig. 4b, the TA spectra of $Cu_{1.4}Ag_{0.6}BiI_5$ NCs film in water exhibit an additional PIA band at ~700 nm after 1 ps delay, possibly ascribed to the fact that the trapped electrons dominate the TA spectra in the range of 600–800 nm, which has been observed for the conventional TiO_2 photocatalyst [36]. This indicates that the photogenerated holes within the $Cu_{1.4}Ag_{0.6}BiI_5$ NCs can first react with the water molecules for oxygen evolution. Fig. 4c compares the TA decays for the $Cu_{1.4}Ag_{0.6}BiI_5$ NCs film measured in air and in water, respectively, monitored at 600 nm. The decays were fitted well with a bi-exponential function and the fitting results are summarized in Table S2. A clear acceleration of the decay was observed for the NCs film in water with a slow component lifetime of 203 ps compared to that ($\gg$5000 ps) of the case in air, indicating the existence of a fast (hundreds of ps) water oxidation reaction component. To further clarify the hole dynamics, we recorded the TA decay of $Cu_{1.4}Ag_{0.6}BiI_5$ NCs film in the presence of Ag^+ ions (provided by $AgNO_3$)

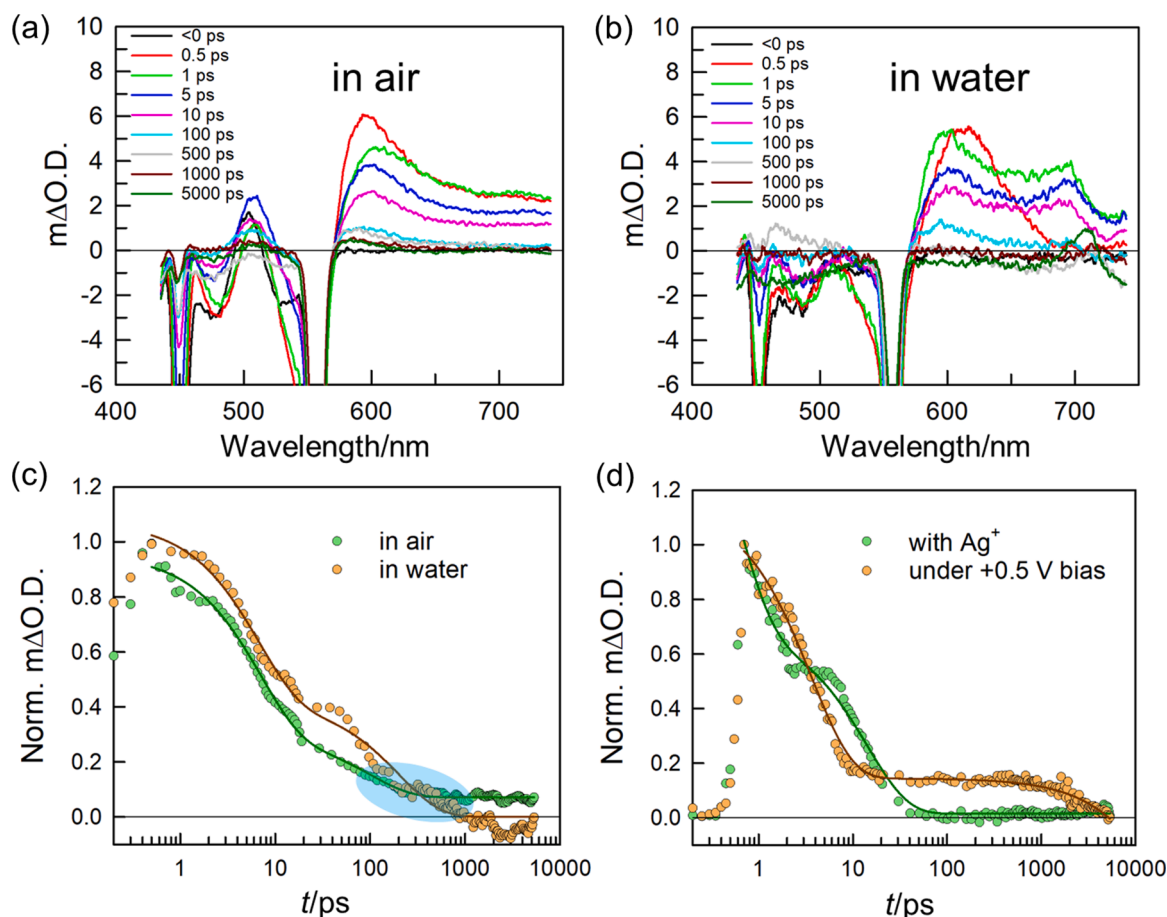**Fig. 4.** Ultrafast TA spectra of $Cu_{1.4}Ag_{0.6}BiI_5$ NCs film (a) in air and (b) in water, excited at 400 nm with an excitation power of 200 μW. Comparison of TA decays of $Cu_{1.4}Ag_{0.6}BiI_5$ NCs film (c) in air and in water, and (d) in the presence of 2 mM $AgNO_3$ aqueous solution and on FTO in 0.1 M $LiClO_4$ aqueous solution with a bias application of +0.5 V vs. Ag/AgCl, respectively, monitored at 700 nm. Solid lines present the fitting results with a bi-exponential function: $\Delta O.D. = A_1 \exp\left(-\frac{t}{\tau_1}\right) + A_2 \exp\left(-\frac{t}{\tau_2}\right)$.

as an electron scavenger in solution as well as under a positive bias (+0.5 V or above)[37] for the creation of an oxidized state (Fig. 4d). Interestingly, a rapid hole decay was observed in $AgNO_3$ solution, likely attributed to the accelerated nongeminate electron-hole recombination upon the excess electrons accumulated in the CB of $Cu_{1.4}Ag_{0.6}BiI_5$ NCs. On the other hand, the charge recombination dynamics are effectively suppressed under the application of $a + 0.5$ V bias, as similarly reported for TiO_2 photoanode-based water oxidation [36]. Our observations hint that the charge carrier (electron-hole) recombination is mainly influenced by the population of electrons in $Cu_{1.4}Ag_{0.6}BiI_5$ NCs. In other words, the photoinduced electron density is supposed to be higher than the hole density, indirectly hinting that the as-synthesized $Cu_{1.4}Ag_{0.6}BiI_5$ NCs possess an n-type semiconductor nature.

In summary, we have reported the first-ever synthesis of $Cu_{1.4}Ag_{0.6}BiI_5$ NCs. Benefiting from the energetically suitable band structures and highly water-resistant property, we fabricated a $Cu_{1.4}Ag_{0.6}BiI_5$ NC-based photoanode without any protective layer for the proof-of-concept PEC water splitting reaction. The $Cu_{1.4}Ag_{0.6}BiI_5$ NC photoanode exhibited an onset potential of -0.05 V_{RHE} and maximum photocurrent density of 4.62 mA cm^2 at 1.23 V_{RHE}, with a 2.94% ABPE, which is the highest record among all reported lead-free perovskites or PIMs-based PEC cells for oxygen evolution. Moreover, our ultrafast transient absorption studies imply that the control of photogenerated electron-hole recombination rates dominates the water oxidation and reduction reactions. We believe that these findings highlight the potential of lead-free semiconducting $Cu_{1.4}Ag_{0.6}BiI_5$ NCs for the future development of low-cost, eco-friendly, and high-performance PEC devices.

Appendix A. Supplementary data

Supporting information to this article can be found online at https://doi.org/xxx

CRediT authorship contribution statement

Maning Liu: Conceptualization, Methodology, Data curation, Validation, Formal analysis, Investigation, Writing – original draft, Project administration, Funding acquisition. **G. Krishnamurthy Grandhi:** Data curation, Formal analysis, Writing – review & editing. **Basheer Al-Anesi:** Data curation, Investigation. **Harri Ali-Löytty:** Data curation, Formal analysis, Writing – review & editing. **Kimmo Lahtonen:** Data curation, Formal analysis. **Roberto Grisorio:** Data curation, Formal analysis. **Paola Vivo:** Formal analysis, Resources, Writing – review & editing, Visualization, Supervision, Funding acquisition.

Declaration of Competing Interest

The authors declare that they have no known competing financial interests or personal relationships that could have appeared to influence the work reported in this paper.

Acknowledgment

Supplementary materials

Supplementary material associated with this article can be found, in the online version, at doi:10.1016/j.electacta.2023.142734.

References

[1] S. Chen, T. Takata, K. Domen, Particulate photocatalysts for overall water splitting, Nat. Rev. Mater. 2 (2017) 1–17.

[2] Z. Wang, C. Li, K. Domen, Recent developments in heterogeneous photocatalysts for solar-driven overall water splitting, Chem. Soc. Rev. 48 (2019) 2109–2125.

[3] J.H. Kim, D. Hansora, P. Sharma, J.W. Jang, J.S. Lee, Toward practical solar hydrogen production-an artificial photosynthetic leaf-to-farm challenge, Chem. Soc. Rev. 48 (2019) 1908–1971.

[4] R. Sathre, J.B. Greenblatt, K. Walczak, I.D. Sharp, J.C. Stevens, J.W. Ager, F. A. Houle, Opportunities to improve the net energy performance of photoelectrochemical water-splitting technology, Energy Environ. Sci. 9 (2016) 803–819.

[5] H. Zhang, Z. Yang, W. Yu, H. Wang, W. Ma, X. Zong, C. Li, a sandwich-like organolead halide perovskite photocathode for efficient and durable photoelectrochemical hydrogen evolution in water, Adv. Energy Mater. 8 (2018), 1800795.

[6] C. Wang, S. Yang, X. Chen, T. Wen, H.G. Yang, Surface-functionalized perovskite films for stable photoelectrochemical water splitting, J. Mater. Chem. A. 5 (2017) 910–913.

[7] M.T. Hoang, N.D. Pham, J.H. Han, J.M. Gardner, I. Oh, Integrated photoelectrolysis of water implemented on organic metal halide perovskite photoelectrode, ACS Appl. Mater. Interface. 8 (2016) 11904–11909.

[8] C. Motta, F. El-Mellouhi, S. Sanvito, Charge carrier mobility in hybrid halide perovskites, Sci. Rep. 5 (2015) 12746.

[9] M. Liu, H. Zhang, D. Gedamu, P. Fourmont, H. Rekola, A. Hiltunen, S.G. Cloutier, R. Nechache, A. Priimagi, P. Vivo, Halide perovskite nanocrystals for next-generation optoelectronics, Small 15 (2019), 1900801.

[10] S. Gonzalez-Carrero, R.E. Galian, J. Pérez-Prieto, Organic-inorganic and all-inorganic lead halide nanoparticles, Opt. Express. 24 (2016) A285.

[11] D. Shi, V. Adinolfi, R. Comin, M. Yuan, E. Alarousu, A. Buin, Y. Chen, S. Hoogland, A. Rothenberger, K. Katsiev, Y. Losovyj, X. Zhang, P.A. Dowben, O.F. Mohammed, E.H. Sargent, O.M. Bakr, Low trap-state density and long carrier diffusion in organolead trihalide perovskite single crystals, Science 347 (2015) 519–522.

[12] H. Choi, S. Seo, J.H. Kim, J.H. Lee, S. Kim, G. Piao, H. Park, K. Lee, S. Lee, An organometal halide perovskite photocathode integrated with a MoS_2 catalyst for efficient and stable photoelectrochemical water splitting, J. Mater. Chem. A. 9 (2021) 22291–22300.

[13] P. Da, M. Cha, L. Sun, Y. Wu, Z.S. Wang, G. Zheng, High-performance perovskite photoanode enabled by Ni passivation and catalysis, Nano Lett. 15 (2015) 3452–3457.

[14] M. Crespo-Quesada, L.M. Pazos-Outón, J. Warnan, M.F. Kuehnel, R.H. Friend, E. Reisner, Metal-encapsulated organolead halide perovskite photocathode for solar-driven hydrogen evolution in water, Nat. Commun. 7 (2016) 1–7.

[15] Y.T. Huang, S.R. Kavanagh, D.O. Scanlon, A. Walsh, R.L.Z. Hoye, Perovskite-inspired materials for photovoltaics and beyond-from design to devices, Nanotechnology 32 (2021) 60.

[16] A. Chakraborty, N. Pai, J. Zhao, B.R. Tuttle, A.N. Simonov, V. Pecunia, Rudorffites and beyond: perovskite-inspired silver/copper pnictohalides for next-generation environmentally friendly photovoltaics and optoelectronics, Adv. Funct. Mater. 32 (2022), 2203300.

[17] S.S. Bhosale, A.K. Kharade, E. Jokar, A. Fathi, S.M. Chang, E.W.G. Diau, Mechanism of photocatalytic CO_2 reduction by Bismuth-based perovskite nanocrystals at the gas-solid interface, J. Am. Chem. Soc. 141 (2019) 20434–20442.

[18] Z. Ma, Z. Shi, D. Yang, F. Zhang, S. Li, L. Wang, D. Wu, Y. Zhang, G. Na, L. Zhang, X. Li, Y. Zhang, C. Shan, Electrically-driven violet light-emitting devices based on highly stable lead-free perovskite $Cs_3Sb_2Br_9$ quantum dots, ACS Energy Lett. (2020) 385–394.

[19] J. Mei, M. Liu, P. Vivo, V. Pecunia, Two-dimensional antimony-based perovskite-inspired materials for high-performance self-powered photodetectors, Adv. Funct. Mater. 31 (2021), 2106295.

[20] A. Hiltunen, N. Lamminen, H. Salonen, M. Liu, P. Vivo, Efficiency improvement for perovskite-inspired $Cs_3Sb_2I_9$ solar cells using P3HT as the hole transport material, Sustain. Energy Fuels. 6 (2022) 217–222.

[21] L.R.V. Buizza, H.C. Sansom, A.D. Wright, A.M. Ulatowski, M.B. Johnston, H. J. Snaith, L.M. Herz, Interplay of structure, charge-carrier localization and dynamics in copper-silver-Bismuth-halide semiconductors, Adv. Funct. Mater. 32 (2022), 2108392.

[22] H.C. Sansom, G. Longo, A.D. Wright, L.R.V. Buizza, S. Mahesh, B. Wenger, M. Zanella, M. Abdi-Jalebi, M.J. Pitcher, M.S. Dyer, T.D. Manning, R.H. Friend, L. M. Herz, H.J. Snaith, J.B. Claridge, M.J. Rosseinsky, Highly absorbing lead-free semiconductor Cu_2AgBiI_6 for photovoltaic applications from the quaternary CuI-AgI-BiI_3 phase space, J. Am. Chem. Soc. 143 (2021) 3983–3992.

[23] F. Zhang, Z. Hu, B. Zhang, Z. Lin, J. Zhang, J. Chang, Y. Hao, Low-temperature solution-processed Cu_2AgBiI_6 films for high performance photovoltaics and photodetectors, ACS Appl. Mater. Interface. 14 (2022) 18498–18505.

[24] G.K. Grandhi, B. Al-Anesi, H. Pasanen, H. Ali-Löytty, K. Lahtonen, S. Granroth, N. Christian, A. Matuhina, M. Liu, V. Pecunia, P. Vivo, Enhancing the microstructure of perovskite-inspired Cu-Ag-Bi-I absorber for efficient indoor photovoltaics, Small 35 (2022), 2203768.

[25] M. Hamdan, A.K. Chandiran, Cs$_2$PtI$_6$ halide perovskite is stable to air, moisture, and extreme pH: application to photoelectrochemical solar water oxidation, Angew. Chemie. 132 (2020) 16167–16172.

[26] X.D. Wang, N.H. Miao, J.F. Liao, W.Q. Li, Y. Xie, J. Chen, Z.M. Sun, H.Y. Chen, D. Bin Kuang, The top-down synthesis of single-layered Cs$_4$CuSb$_2$Cl$_{12}$ halide perovskite nanocrystals for photoelectrochemical application, Nanoscale 11 (2019) 5180–5187.

[27] B. Yang, F. Hong, J. Chen, Y. Tang, L. Yang, Y. Sang, X. Xia, J. Guo, H. He, S. Yang, W. Deng, K. Han, Colloidal synthesis and charge-carrier dynamics of Cs$_2$AgSb$_{1−y}$Bi$_y$X$_6$ (X: Br, Cl; 0 ≤y ≤1) double perovskite nanocrystals, Angew. Chemie - Int. Ed 58 (2019) 2278–2283.

[28] M. Liu, S.K. Matta, H. Ali-Löytty, A. Matuhina, G.K. Grandhi, K. Lahtonen, S. P. Russo, P. Vivo, Moisture-assisted near-UV emission enhancement of lead-free Cs$_4$CuIn$_2$Cl$_{12}$ double perovskite nanocrystals, Nano Lett. 22 (2022) 311–318.

[29] A. Adappattu Ramachandran, B. Krishnan, D. Avellaneda Avellaneda, M. Isabel Mendivil Palma, J. Amilcar Aguilar Martinez, S. Shaji, Development of lead-free Cu$_2$BiI$_5$ rudorffite thin films for visible light photodetector application, Appl. Surf. Sci. 564 (2021), 150438.

[30] R.D. Shannon, Revised effective ionic radii and systematic studies of interatomic distances in halides and chalcogenides, Acta Crystallogr. Sect. A. 32 (1976) 751–767.

[31] J. Shamsi, A.S. Urban, M. Imran, L. De Trizio, L. Manna, Metal halide perovskite nanocrystals: synthesis, post-synthesis modifications, and their optical properties, Chem. Rev. 119 (2019) 3296–3348.

[32] H.C. Sansom, L.R.V. Buizza, M. Zanella, J.T. Gibbon, M.J. Pitcher, M.S. Dyer, T. D. Manning, V.R. Dhanak, L.M. Herz, H.J. Snaith, J.B. Claridge, M.J. Rosseinsky, Chemical control of the dimensionality of the octahedral network of solar absorbers from the CuI-AgI-BiI$_3$ phase space by synthesis of 3D CuAgBiI$_5$, Inorg. Chem. 60 (2021) 18154–18167.

[33] H. Idriss, The elusive photocatalytic water splitting reaction using sunlight on suspended nanoparticles: is there a way forward? Catal. Sci. Technol. 10 (2020) 304–310.

[34] L.R.V. Buizza, A.D. Wright, G. Longo, H.C. Sansom, C.Q. Xia, M.J. Rosseinsky, M. B. Johnston, H.J. Snaith, L.M. Herz, Charge-carrier mobility and localization in semiconducting Cu$_2$AgBiI$_6$ for photovoltaic applications, ACS Energy Lett 6 (2021) 1729–1739.

[35] L.M. Herz, Charge-carrier dynamics in organic-inorganic metal halide perovskites, Annu. Rev. Phys. Chem. 67 (2016) 65–89.

[36] H. Liu, M. Liu, R. Nakamura, Y. Tachibana, Primary photocatalytic water reduction and oxidation at an anatase TiO$_2$ and Pt-TiO$_2$ nanocrystalline electrode revealed by quantitative transient absorption studies, Appl. Catal. B Environ. 296 (2021), 120226.

[37] M. Liu, H. Ali-Löytty, A. Hiltunen, E. Sarlin, S. Qudsia, J. Smått, M. Valden, P. Vivo, Manganese doping promotes the synthesis of bismuth-based perovskite nanocrystals while tuning their band structures, Small 17 (2021), 2100101.

[38] X. Luo, Y. Han, Z. Chen, Y. Li, G. Liang, X. Liu, T. Ding, C. Nie, M. Wang, F. N. Castellano, K. Wu, Mechanisms of triplet energy transfer across the inorganic nanocrystal/organic molecule interface, Nat. Commun. 11 (2020) 1–10.

[39] X. Yan, Z. Huang, S. Sett, J. Oh, H. Cha, L. Li, L. Feng, Y. Wu, C. Zhao, D. Orejon, F. Chen, N. Miljkovic, Atmosphere-mediated superhydrophobicity of rationally designed micro/nanostructured surfaces, ACS Nano 13 (2019) 4160–4173.

[40] T.G. Kim, J.H. Lee, G. Hyun, S. Kim, D.H. Chun, S.J. Lee, G. Bae, H.S. Oh, S. Jeon, J. H. Park, Monolithic lead halide perovskite photoelectrochemical cell with 9.16% applied bias photon-to-current efficiency, ACS Energy Lett. 7 (2022) 320–327.

[41] M.Z. Yang, Y.F. Xu, J.F. Liao, X.D. Wang, H.Y. Chen, D. Bin Kuang, Constructing CsPbBr$_x$I$_{3-x}$ nanocrystal/carbon nanotube composites with improved charge transfer and light harvesting for enhanced photoelectrochemical activity, J. Mater. Chem. A. 7 (2019) 5409–5415.

[42] H. Peng, L. Xu, Y. Sheng, W. Sun, Y. Yang, H. Deng, W. Chen, J. Liu, Highly conductive ligand-free Cs$_2$PtBr$_6$ perovskite nanocrystals with a narrow bandgap and efficient photoelectrochemical performance, Small (2021) 17.

[43] B. Yang, K. Han, Ultrafast dynamics of self-trapped excitons in lead-free perovskite nanocrystals, J. Phys. Chem. Lett. 12 (2021) 8256–8262.